Thin–Walled Structures 228 (2026) 115088

Contents lists available at ScienceDirect

Thin-Walled Structures

journal homepage: www.elsevier.com/locate/tws

Full length article

Isotropic auxetic trigonal symmetry tessellations designed for FDM printing infill patterns

Reza Moghimimonfared, Andrea Spaggiari, Luke Mizzi *

Department of Sciences and Methods for Engineering, University of Modena and Reggio Emilia, Reggio Emilia, Italy

ARTICLE INFO

Keywords:
Auxetic metamaterials
Poisson's ratio
Additive manufacturing
Infill Patterns

ABSTRACT

Mechanical metamaterials derived from Euclidean polygonal tessellations constitute a novel class of architected materials capable of exhibiting a broad spectrum of mechanical properties, including auxeticity. In this work, new monohedral and dihedral tessellations derived from a Euclidean hexagonal tessellation system possessing trigonal rotational symmetry were designed through targeted structural modifications of the original tessellation. A parametric analysis was carried out on these tessellations using finite element (FE) simulations in order to evaluate the Poisson's ratios and effective Young's moduli, followed by experimental tests on various additively-manufactured prototypes to validate the results predicted by the FE simulations. The results obtained show that these new transversely-isotropic tessellations have the capability of exhibiting the entire spectrum of two-dimensional isotropic Poisson's ratios ($-1 < \nu < +1$) as well as a wide range of Young's moduli. The representative unit cells of these tessellations are also relatively small (compared to other irregular monohedral and dihedral networks) and highly porous, which coupled with the inherent tuneability in mechanical properties and isotropic behaviour, makes them ideal for implementation as infill patterns for Fused-Deposition Method (FDM) additively-manufactured components with low volume fractions.

1. Introduction

Additive Manufacturing (AM) is a manufacturing process that fabricates components directly from 3D model data by depositing material layer by layer, differing fundamentally from conventional subtractive or formative manufacturing techniques [1]. The emergence of Additive Manufacturing technology has driven a paradigm shift from the traditional principle of "design for manufacturing" toward "manufacturing for design," with a focus on product functionality [2]. Building on this capability, this manufacturing technique enables the production of highly complex, topologically optimized, lightweight, and lattice-based structures as well as functionally graded materials (multi-material AM) that are often unattainable with conventional manufacturing methods, while minimizing finishing work and significantly reducing material waste, making it a more sustainable alternative to traditional subtractive techniques [2–6].

In the present study, we focus on the FDM manufacturing technology, which is one of the most widely used AM techniques for fabricating models, prototypes, and functional products due to its simplicity, cost-effectiveness, and versatility in processing thermoplastic polymers. In this process, thermoplastic filaments are heated slightly beyond their glass transition or melting temperature in an extruder and then delivered to a nozzle that precisely controls the flow, building parts layer by layer [7–9]. FDM offers advantages such as low cost, wide material availability, and ease of use, making it highly suitable for both research and industrial prototyping [7–9]. This AM technique has found applications across a broad spectrum of industries, including aerospace, automotive, marine, biomedical, sport, sensors, and construction, due to its ability to produce lightweight structures, customized components, and functional prototypes with high precision [7–12]. Several factors influence the FDM 3D printing process and, consequently, the quality of fabricated parts—such as material type, layer height, layer adhesion, nozzle temperature, printing speed, support structure, infill density, and infill design [12–19]. Among these, infill design plays a particularly critical role, with standard geometries such as line, rectilinear, triangular, grid, honeycomb, cubic, and gyroid patterns, among others, each offering distinct trade-offs between strength, flexibility, and efficiency. Infill design also significantly affect the mechanical performance, weight, material consumption, and printing time of the final part [20–23].

* Corresponding author.
E-mail address: luke.mizzi@unimore.it (L. Mizzi).

https://doi.org/10.1016/j.tws.2026.115088
Received 12 February 2026; Received in revised form 15 April 2026; Accepted 7 May 2026
Available online 9 May 2026
0263-8231/© 2026 The Author(s). Published by Elsevier Ltd. This is an open access article under the CC BY license (http://creativecommons.org/licenses/by/4.0/).

While numerous studies have focused on the effects of commercially available infill patterns in FDM machines on the characteristics of fabricated parts, there may be considerable potential in exploring auxetic metamaterial geometries as alternative infill patterns, since they possess unconventional properties and have not yet been implemented in this context. Auxetic mechanical metamaterials exhibit negative Poisson's ratio, meaning they become wider when stretched and thinner when compressed, in contrast to conventional materials [24–27]. This unusual behavior, resulting from their distinct geometrical arrangements, leads to remarkable properties such as enhanced energy absorption [28], superior indentation and impact resistance [29], and improved fracture toughness [30]. Auxetic metamaterials can generally be broadly classified into re-entrant [31–34], chiral [35–40], rotating rigid units [41–43] and origami structures [44–46]. These general mechanistic classifications each incorporate various forms and configurations encompassing various symmetry classes and topologies, including both 2D and 3D systems [40,47–50]. Furthermore, other advanced classes including fractal/hierarchical geometries [51–53], functionally-graded architectures [54], hybrid mixed-mode systems [55] and disordered/aperiodic frameworks [56–58] can also be formed to obtain further advanced functionalities over conventional materials. Auxetic metamaterials have already demonstrated to be promising for implementation in applications in fields such as biomedical implants [59,60], protective and sport equipment with high energy absorption characteristics [28], aerospace engineering [61], and soft robotics [62], suggesting that their integration as 3D printing infill patterns may enhance the capability of this manufacturing technology to produce lightweight yet high-performance printed parts.

On this basis, the present work aims to explore how auxeticity may be attained from various tessellatable structures through a wide-ranging parametric study, with the goal of identifying configurations with variable mechanical properties, including unconventional behaviours such as a negative Poisson's ratio that could be implemented in 3D printing technology as potential infill patterns. Specifically, we considered tessellations which exhibit in-plane isotropy; a property which is highly desirable for infill patterns; coupled with a relatively small representative unit cell. These include a) a hexagonal cellular tessellation [63] with trigonal rotational symmetry, which following a series of targeted structural modifications, can yield three additional derived configurations: b) Design I, a monohedral dodecagonal tessellation; c) Design II, a dihedral tessellation composed of pentagons and triangles; and d) Design III, a dihedral tessellation composed of nonagons and triangles. Using Finite Element (FE) simulations, various configurations of these systems were analysed, followed by an experimental validation on exemplars produced using FDM additively manufacturing. Through this study, these new tessellations, each of which retains the rotational trigonal symmetry and unit cell size of the original hexagonal system, have been demonstrated to possess the capability of exhibiting a wide range of mechanical properties, including the entire spectrum of isotropic Poisson's ratio, and could potentially be used as an infill pattern for the attainment of on-demand micromechanical properties of additively-manufactured components.

2. Methodology

In this section, the methodology used to design the new tessellations through modifications of the original hexagonal geometry [63] possessing trigonal rotational symmetry is described. This is followed by an explanation of the parametric linear Finite Element (FE) simulations conducted using periodic boundary conditions (PBCs) to evaluate the Poisson's ratios and effective Young's moduli of the designed structures. Finally, the experimental procedure used to validate the results obtained from the FE simulations is presented in detail. Through this organized methodology, we aim to obtain a comprehensive understanding of the mechanical properties of the proposed structures.

2.1. Design the targeted structures with specified unit cell

As previously stated, the three configurations designed in this study—Design I, Design II, and Design III—are derived from a hexagonal tessellation with trigonal rotational symmetry. As depicted in Fig. 1a, the original hexagon is composed of three pairs of consecutive sides with side lengths denoted as i, j, and k, arranged such that the angle between each pair of identical lengths is 120°, while the remaining three interior angles vary based on geometric constraints. The geometric features of this hexagon, as well as its realizable area as a function of the side lengths, are described in detail in [63] and are also included in the Supplementary Information. The methodology used to design the proposed configurations exhibiting trigonal rotational symmetry is outlined below:

i. **Design I.** These structures were obtained by removing both sides of length i from the original hexagon. This modification transforms the original hexagon into an open-ended four-sided shape. However, following the rotational trigonal symmetry rotational replication, the original monohedral hexagonal tessellation is converted into a monohedral dodecagonal tessellation (see Fig. 1b).
ii. **Design II.** These structures were obtained by removing both sides of length j from the original hexagon and adding a diagonal connecting their endpoints (denoted as jj). These modifications transform the original hexagon into a pentagon. However, following the trigonal rotational symmetry replication, the original monohedral hexagonal tessellation is converted to a dihedral tessellation consisting of a pentagon and a triangle (see Fig. 1c).
iii. **Design III.** These structures were obtained by removing four sides of the hexagon—two of length i and two of length j—and adding a diagonal connecting the endpoints of the two removed j sides (denoted as jj). These modifications transform the original hexagon into an open-ended shape with three sides. However, following the trigonal rotational symmetry replication, the original monohedral hexagonal tessellation is converted into a dihedral tessellation consisting of a nonagon and a triangle (see Fig. 1d).

It is worth noting that in Designs II and III, when $j = i + k$, the resulting structure forms a triangular tessellation, which deviates from the typical configurations of Design II (pentagon + triangle) and Design III (nonagon + triangle). These configurations (which are extremely few) arise as a result of the boundaries of the realizability conditions for these tessellations and given that they represent different polygonal tessellations, were excluded from the current study. It is also important to specify that for all three designs studied in this work, the side length variables i, j and k are interchangeable and that the same geometries are effectively obtained from the same combination of variables.

2.2. Parametric FE analysis using periodic boundary conditions

To examine the mechanical properties—specifically, Poisson's ratio and effective Young's modulus—of the newly designed structures, a parametric study was conducted using ANSYS Mechanical APDL. For each of these three designs, a wide range of structures was simulated across three subsets, with variables defined as follows:

A) ***i*-constant:** The value of i was kept constant as 24 mm, while j and k varied between 1.2 mm (0.05i) and 84 mm (3.5i) in increments of 1.2 mm (0.05i).
B) ***j*-constant:** The value of j was kept constant as 24 mm, while i and k varied between 1.2 mm (0.05j) and 84 mm (3.5j) in increments of 1.2 mm (0.05j).

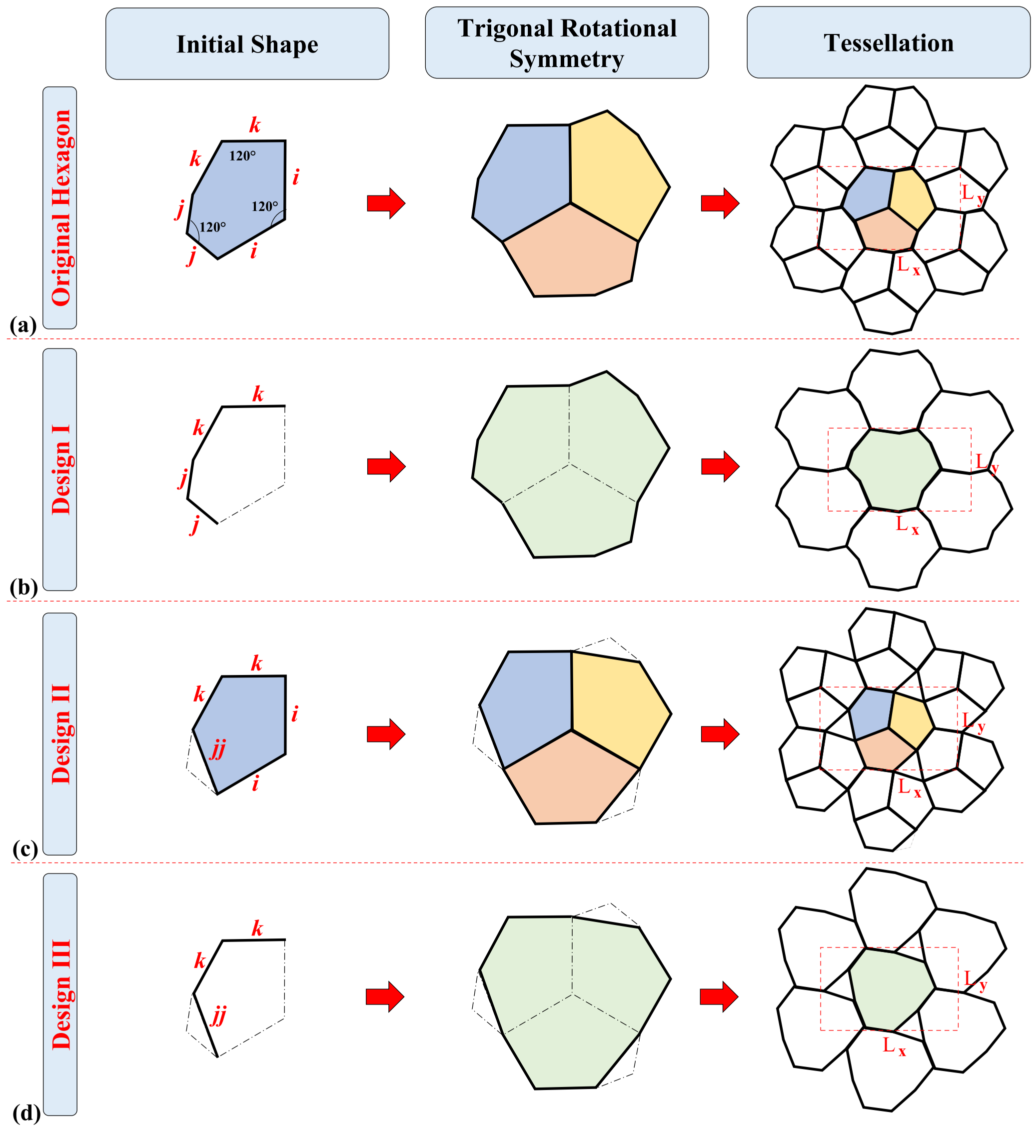

Fig. 1. Methodology for designing the newly developed hexagon-based structures: a) The original hexagon with trigonal rotational symmetry, constructed from three pairs of identical consecutive side lengths, denoted as *i*, *j*, and *k*, arranged such that the angles between identical lengths are 120°, while the three remaining angles vary; b) Design I, obtained by removing both sides of length *i* from the original hexagon; c) Design II, formed by removing both sides of length *j* and adding a diagonal connecting their endpoints, denoted as *jj*; d) Design III, generated by removing four sides—two of length *i* and two of length *j*—and adding a diagonal connecting the endpoints of the removed *j* sides, also denoted as *jj*.

C) ***k*-constant:** The value of k was kept constant as 24 mm, while i and j varied between 1.2 mm (0.05k) and 84 mm (3.5k) in increments of 1.2 mm (0.05k).

By considering these three subsets, we aimed to ensure a comprehensive investigation of the mechanical properties of the three aforementioned designs. A total of nine sets of parametric simulations were conducted, each adhering to the geometric constraints necessary to maintain a realizable shape (these conditions are detailed in [63]). Within the FE simulations process, the representative unit cells (RUCs) of the designed structures were meshed using BEAM189 elements with a constant rectangular cross-section, defined by an in-plane thickness (t) of 0.1 mm and an out-of-plane depth (d) of 1 mm. After performing mesh convergence analysis testing, the element size was defined as 24/120 to ensure a minimum of six elements along the shortest side length, i.e., 1.2 mm. The BEAM189 element is defined according to Timoshenko beam theory, incorporating shear deformation effects, making it suitable for analyzing slender to moderately thick beam structures. The parameters detailed in the subsets defined above all result in systems with ligaments which adhere to this classification, making BEAM elements the natural choice for simulation of these metamaterial networks with optimal computational efficiency. This element consists of a quadratic three-node beam, with its default configuration presenting six degrees of freedom at each node, encompassing three translational and three rotational motions [64]. The constitutive material properties were defined as linear isotropic ABS material, characterized by a Young's modulus of $E = 1$ GPa and Poisson's ratio of $\nu = +0.3$. For each system, the RUC was defined by the lengths L_x and L_y, which are determined as a function of the side lengths i, j, and k (shown in Eqs. 1 and 2) [63]. The schematic configuration of the rectangular RUC for the designed structures is shown in the rightmost column of Fig. 1 and for a given set of i, j and k is identical for the new designs (I, II and III) as well as the original configuration. This RUC was used to perform linear FE simulations by applying appropriate periodic boundary conditions (PBCs) and in-plane loading systems in both the x and y-directions. Since these geometries lack an axis of mirror symmetry, PBCs were implemented through a series of specific constraint equations on the corresponding nodes located on opposite edges of the unit cell, ensuring correlation between their rotational and translational motions. The system was completely fixed (i.e. $U_x = 0$ and $U_y = 0$) from a single point in the bottommost edge of the RUC and fixed in the x-direction only ($U_x = 0$) from the corresponding node of the upper edge in order to ensure that there is no rigid body motion and that the system remains aligned with the global y-axis throughout deformation. The FE simulation technique employed in this study, using PBCs with the BEAM element, is based on the generic implementation of boundary conditions [65,66] and described in detail in [63].

$$L_x = \sqrt{i^2 + k^2 - 2ik\cos\left(\arccos\left(\frac{i^2 + k^2 - j^2}{2ik}\right) + \frac{\pi}{3}\right)} + \sqrt{i^2 + j^2 - 2ij\cos\left(\arccos\left(\frac{i^2 + j^2 - k^2}{2ij}\right) + \frac{\pi}{3}\right)} + \sqrt{j^2 + k^2 - 2jk\cos\left(\arccos\left(\frac{j^2 + k^2 - i^2}{2jk}\right) + \frac{\pi}{3}\right)} \tag{1}$$

$$L_y = L_x \tan\left(\frac{\pi}{6}\right) \tag{2}$$

2.3. Sample preparation and experimental test

To validate the results obtained from the FE simulations, one prototype of each design (I, II, and III), along with one of their base hexagonal tessellations, was fabricated to conduct experimental testing. The length combinations were identical across all four prototypes, with $i = 20$ mm, $j = 14$ mm, and $k = 6$ mm. The printed prototypes consist of three RUCs in horizontal direction and five RUCs in the vertical direction, with rectangular blocks (10 mm in height) added to the top and bottom edges of the 3×5 RUCs system. These blocks facilitate proper placement of the specimens within the tensile testing machine and promote uniform distribution of the applied load during testing. The overall horizontal and vertical dimensions of the prototypes, including the rectangular blocks, are 160 mm and 174 mm, respectively. Images of the fabricated prototypes are shown in Fig. 2. The in-plane thickness of the ligaments was set to 1 mm, and a fillet with a radius of 0.25 mm was applied at the ligament intersections. Additionally, the out-of-plane thickness of the prototypes was set to 20 mm. The prototypes were fabricated using a Bambu Lab X1 3D printing machine with ABS material and 100% infill.

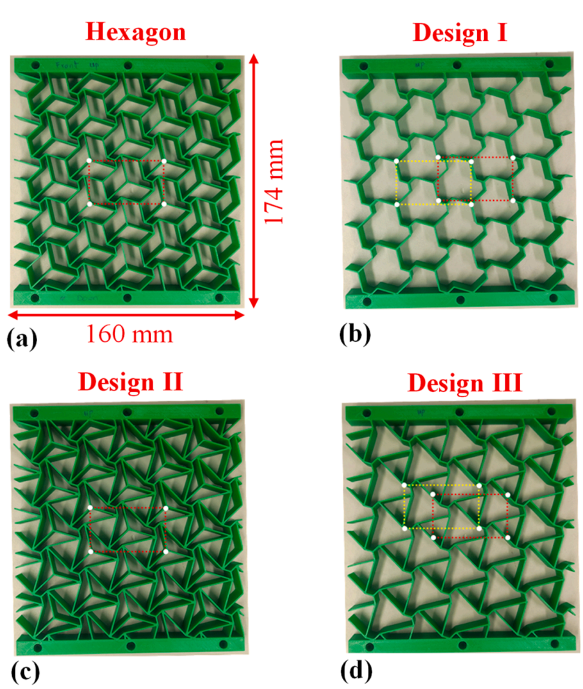

Fig. 2. Fabricated AM prototypes with length combinations of $i = 20$ mm, $j = 14$ mm, and $k = 6$ mm, along with the compression test setup: a) hexagonal structure, b) dodecagonal structure (Design I), c) pentagonal-triangular structure (Design II), d) nonagonal-triangular structure (Design III).

Prior to carrying out the experimental tests, all prototypes were marked with white points on either four or eight vertices, depending on the presence or absence of the central RUC vertices. Specifically, four points were marked on the vertices of the central RUC for the original (see Fig. 2a) hexagon and Design II (see Fig. 2c) structures, whereas eight points were marked near the central RUC for Design I and Design III structures (see Fig. 2b and d), in which the central RUC vertices are inherently removed by the designs. These marked points were then tracked at each loading step (image) using image processing techniques, allowing Poisson's ratios of each system to be calculated. For this purpose, the average length and width of the marked rectangular RUCs prior to loading were taken as the initial reference lengths, and variations in these lengths at each step were used to determine the corresponding strains and Poisson's ratios in both the x and y-directions. Finally, all prototypes were subjected to a *quasi*-static compressive loading condition of 10% global strain using a Galdabini® universal tensile testing machine equipped with a 5000 N load cell, at a crosshead speed of 5 mm/min. In order to perform an accurate comparison between the experimental results and the simulation predictions, an additional set of non-linear geometric simulations using PLANE183 elements was carried out on geometries corresponding to the experimental prototypes. The PLANE183 element models the material as a two-dimensional system, incorporating a more realistic representation of ligament connectivity and representing with a higher degree of accuracy and precision the localised stress distributions within the structure. This ensures a more effective modelling of the interconnection regions where the ligaments meet and provides a more realistic and direct comparison to the experimentally tested prototypes, particularly with respect to capturing the influence of geometric nonlinearities. Therefore, separate nonlinear finite element simulations using PLANE183 elements were performed for the experimentally fabricated specimens, which had an in-plane ligament thickness of 1 mm and an out-of-plane thickness of 20 mm, consistent with the printed prototypes. This simulation mode allows for a more thorough analysis of the localized von Mises strain distributions and captures more accurately the stresses and deformations at the vertices of the truss systems. Two sets of additional FE simulations were carried out; the first set under periodic boundary conditions, similar to the beam element simulations, while the second set under finite loading conditions analogous to the experimental tests (see Supplementary Information). In the latter case, the Poisson's ratio was extracted from the central representative unit cell, similar to the experimental tests.

3. Results and discussion

The results obtained from the parametric study conducted using FE simulation are presented in this section in terms of the Poisson's ratio and effective Young's modulus. The effective Young's modulus (E^*) for each structure was determined by normalizing the simulated Young's modulus (E_{meta}), obtained from the FE analysis, with respect to the predefined modulus of the base material (E_{mat}), which is 1 GPa (as obtained from tests on 3D-printed dogbone samples shown in the Supplementary Information). It can thus be defined as follows:

$$E^* = \frac{E_{meta}}{E_{mat}} \tag{3}$$

Subsequently, the experimental results obtained from the compression tests are presented, which validate the FE findings.

3.1. Linear finite element simulations

In this section, the results obtained for each tessellation from the linear FE simulations are discussed separately. At this point, it is important to highlight that due to their inherently trigonal rotational symmetry architecture, all tessellations studied in this work are transversely-isotropic. This is confirmed by the results obtained for loading in the *x*- and *y*-directions, which are identical, and therefore, all results for mechanical properties are presented in terms of a single Poisson's ratio and effective Young's modulus.

3.1.1. Design I

The contour plots of Poisson's ratios and effective Young's moduli as function of variable side lengths for Design I are shown in Fig. 2. These results were obtained from the parametric FE simulations by considering *i*-, *j*-, and *k*-constant, respectively, whilst varying the remaining two variables. The design space was chosen in order to ensure that all combinations of the geometrical design were evaluated.

It is clearly evident from the plots in Fig. 3 that the Poisson's ratio varies significantly as a function of the length variables, *i*, *j* and *k*. The plots for the sets with *j*-constant and *k*-constant are identical since there is no distinction between the resultant tessellations formed by keeping *j* or *k* constant when the side lengths *i* are removed. This observation is further reflected in the i-constant set shown in Fig. 3a and b, which exhibits symmetrical behavior with respect to the line $k/i = j/i$ for both Poisson's ratio and effective Young's modulus. This symmetry indicates that configurations mirrored about this line possess identical mechanical properties, as they correspond to geometrically equivalent dodecagonal tessellations with constant *i*, obtained through the interchange of the length parameters *j* and *k*.

As shown in Fig. 3a, c and e, the Poisson's ratio for Design I varies from -0.55 to $+1$. The most auxetic structures are obtained when *k* and $j >> i$ and $k - j = i$, with -0.55 being the actual limit within the boundary limits of realisability for the tessellation (see reference [63] for further details on the mathematical realizability limits of this tessellations). In the plots shown in Fig. 3c and e, this limit is obtained for the smallest *i* values (i.e. when $i/k \to 0$ and when $i/j \to 0$), while in Fig. 3a, it is obtained as k/i and $j/i \to \infty$, with the lowest values in the plot, shown as points D and F, exhibiting a value of -0.48.

Two examples of Design I systems showing a negative and positive Poisson's ratios are shown in Fig. 4. In the negative Poisson's ratio system, it is evident that the smallest ligaments (in this case the *j*-ligaments) are rotating as a whole triangle resulting in a rotating mechanism, hence the auxetic behaviour. On the other hand, in the second system with a positive Poisson's ratio, it is clearly evident that the system is deforming predominantly through flexure of the ligaments similar to a regular hexagon [67].

In terms of effective Young's modulus, the results obtained indicated that, as expected, the systems with the shortest ligaments are the stiffest. Given that the *i*-ligaments are not present in Design I, it is unsurprising that the stiffness of the systems depend almost entirely on the size of the *j*- and *k*-ligaments and this is reflected in the trends shown in the plots in Fig. 3b, d and f. In the numerical simulations set, the largest effective Young's modulus is obtained for the configurations with the smallest k/i and j/i values in Fig. 3b, with a value of 1.66×10^{-7}.

To provide further insight into Design I, the trends of Poisson's ratio

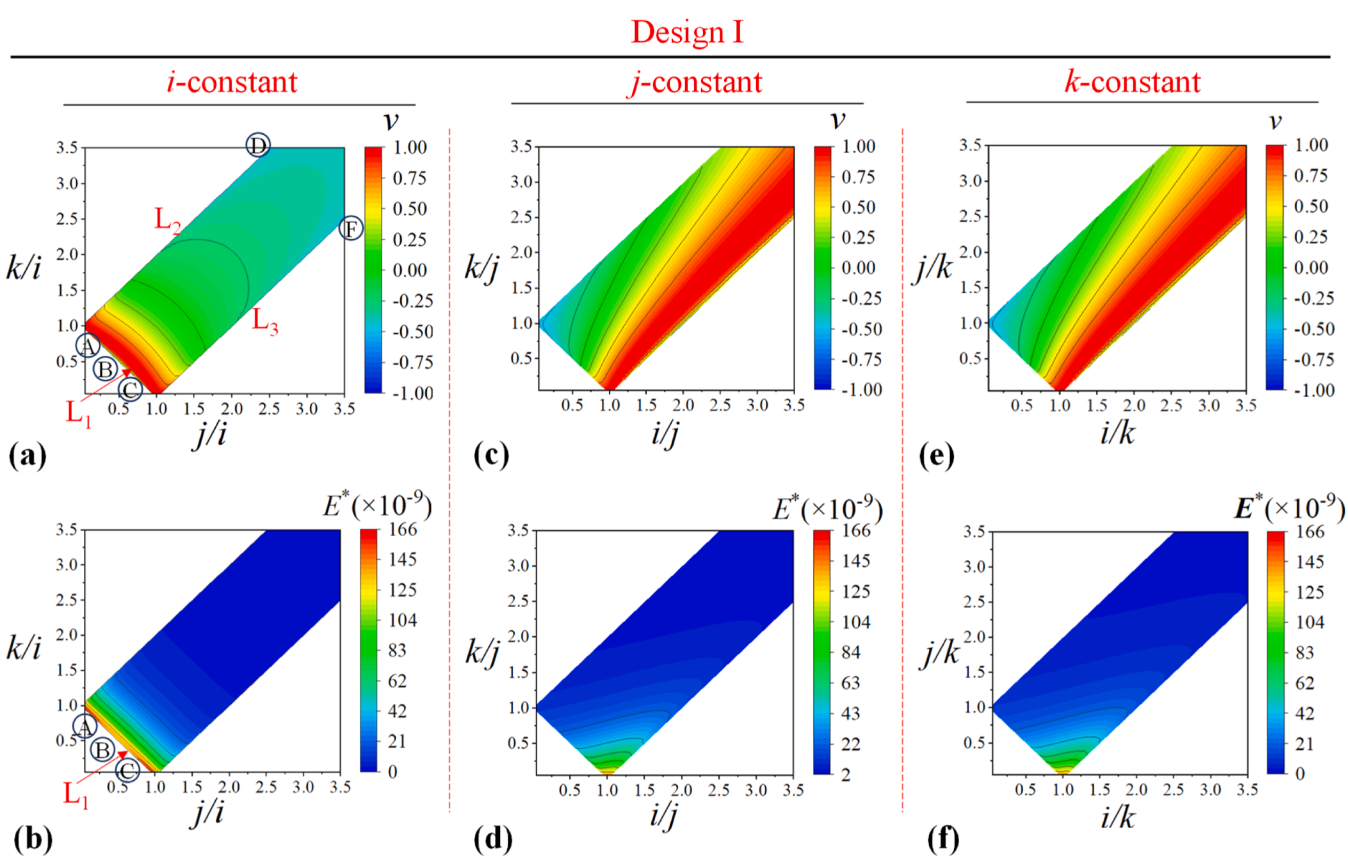

Fig. 3. Variation of Poisson's ratio and effective Young's modulus as functions of the variable side lengths for Design I, considering *i*-, *j*-, and *k*-constant set: a) Poisson's ratio of the *i*-constant set, with a minimum value of -0.48 for $j/i = 2.5$, $k/i = 3.5$ and $j/i = 3.5$, $k/i = 2.5$; b) Effective Young's modulus of the *i*-constant set, with a maximum value of 166×10^{-9} for $j/i = 0.05$, $k/i = 0.95$, and $j/i = 0.95$, $k/i = 0.05$; c) Poisson's ratio of the *j*-constant set, with a minimum value of -0.55 for $i/j = 0.05$, $k/j = 0.95$; $i/j = 0.05$, $k/j = 1.05$; $i/j = 0.1$, $k/j = 0.9$; $i/j = 0.1$, $k/j = 1.1$; d) Effective Young's modulus of the *j*-constant set, with a maximum value of 145×10^{-9} for $i/j = 0.95$, $k/j = 0.05$; e) Poisson's ratio of *k*-constant set, with a minimum value of -0.55 for $i/k = 0.05$, $j/k = 0.95$; $i/k = 0.05$, $j/k = 1.05$; $i/k = 0.1$, $j/k = 0.9$; $i/k = 0.1$, $j/k = 1.1$; f) Effective Young's modulus of *k*-constant set, with a maximum value of 145×10^{-9} for $i/k = 0.95$, $j/k = 0.05$.

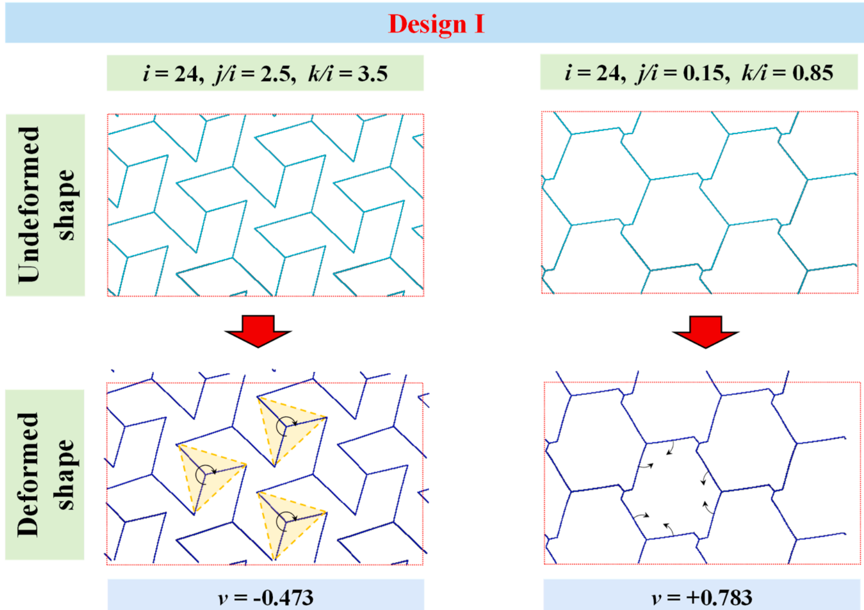

Fig. 4. Images showing the undeformed and deformed shapes of two Design I systems with *i*-constant showing a negative and positive Poisson's ratio. The orange triangles and arrows indicate the direction of deformation of the ligaments. The systems are shown with 2×2 representative unit cells in order to demonstrate clearly the deformation mechanism.

and effective Young's modulus along the boundary line L_1 (defined by $j/i + k/i = 1$) with *i*-constant, along with the geometrical configurations of three representative structures labeled A, B, and C on this line, are presented in Fig. 5. The configurations represented on this line pertain to the systems with the largest effective Young's modulus, all of which have a positive Poisson's ratio. As shown in Fig. 4a, the stiffness of the systems increases as the configuration moves away from the midpoint (point B) toward either boundaries (points A and C). This is due to the fact that one set of ligaments becomes very short, thereby becoming stiffer per standard beam theory [68]. As shown in Fig. 4, these systems deform predominantly through flexure, hence the positive Poisson's ratio.

3.1.2. Design II

Fig. 6 illustrates contour plots of the parametric FE results for Poisson's ratio and effective Young's modulus as functions of the variable side lengths for Design II. The first observation which must be noted is that the *i*-constant and *k*-constant simulation sets exhibit mirror symmetry with respect to each other. This is due to the fact that the resultant structures are identical to each other, thus demonstrating identical mechanical properties. Additionally, the *j*-constant simulations display symmetrical behavior relative to the line $i/j = k/j$. Both of these general observations are consistent with the fundamental geometry of Design II. It is also important to mention that the configurations on the boundary line $j = i + k$ are not included in this result set since, although realizable, they conform to another tessellation type consisting of a trihedral tessellation made up of three differently sized triangles.

As shown in Fig. 6a, c, and e, Poisson's ratio for Design II is generally close to $+1$ for nearly all configurations. However, at the boundaries of the design space (i.e. $k = i + j$ and $i = j + k$), the Poisson's ratio changes drastically, varying from -0.85 to $+1$. This is congruent with the results observed for the original hexagonal tessellation [63], however in this case the Poisson's ratio can reach significantly more negative values beyond the previous limit of -0.22. In the numerical design space, the minimum value obtained was -0.85 for the configurations with $j/i = 0.95$, $k/i = 0.05$ and $i/k = 0.05$, $j/k = 0.95$, however it is possible to go beyond this limit and arrive close to -1 for configurations which correspond to $k = i + j$ and $k >> i$ or $i >> k$. In order to confirm this, an additional simulation was carried out for a configuration with $i = 24$, $j/i = 0.998$, $k/i = 0.002$ and $t/i = 2.08 \times 10^{-4}$ (the thickness of the ligaments was changed in order to ensure that the system could still be accurately simulated using beam elements). The resultant structure is shown in Fig. 7 and has a Poisson's ratio of – 0.96.

It is clearly evident from Fig. 7 that the negative Poisson's ratio configuration exhibits a deformation mechanism which is similar to a chiral honeycomb [69], with vertices with 9 connections showing a significant degree of rotation, while the vertices with 3 connections show less rotation in the opposite direction. This results in an extremely negative Poisson's ratio close to -1. On the other hand the positive Poisson's ratio architecture has a tessellation shape which is very similar to a rhombile tiling which is known to exhibit a highly positive isotropic Poisson's ratio [36]. The configurations on the boundary lines $k = i + j$ and $i = j + k$ migrate from one limit to the other, hence these systems can exhibit the entire spectrum of 2D isotropic Poisson's ratio, i.e. $-1 < \nu < +1$. This variation is shown in Fig. 8, where the transition in Poisson's ratio and Young's modulus along the line along boundary line L_1, defined by $k/i + j/i = 1$ for *i*-constant is plotted. The corresponding structures for combinations A, B, and C are shown in Fig. 8b-d, respectively. transitioning from Structure A to Structure C—where larger triangles are formed—leading to an increase in effective Young's modulus and a decrease in Poisson's ratio. It is worth noting that the maximum Young's modulus was obtained for architectures possessing a positive Poisson's ratio of $+0.93$, with the following configuration: $j/i = 1$, $k/i = 0.05$. This configuration does not fall on the boundary line and yielded an effective Young's modulus of 3.69×10^{-4}.

3.1.3. Design III

The contour plots of Poisson's ratios and effective Young's modulus as functions of their variable side lengths for Design III are illustrated in Fig. 9. Similar to Design II, the boundary line $j = i + k$ results in a separate triangular tessellation that differs from the typical configurations of Design III. Consequently, these boundary lines in the contour plots are excluded from the overall analysis. It is immediately apparent that unlike Design I and II, the three plots do not show any symmetry relations. This is due to the fact that for this tessellation type, the sides *i*, *j* and *k* are not interchangeable since, as shown in Fig. 1, different variations are applied to each set of sides once creating Design III from the original trigonal symmetry hexagonal tessellations, i.e. the sides with

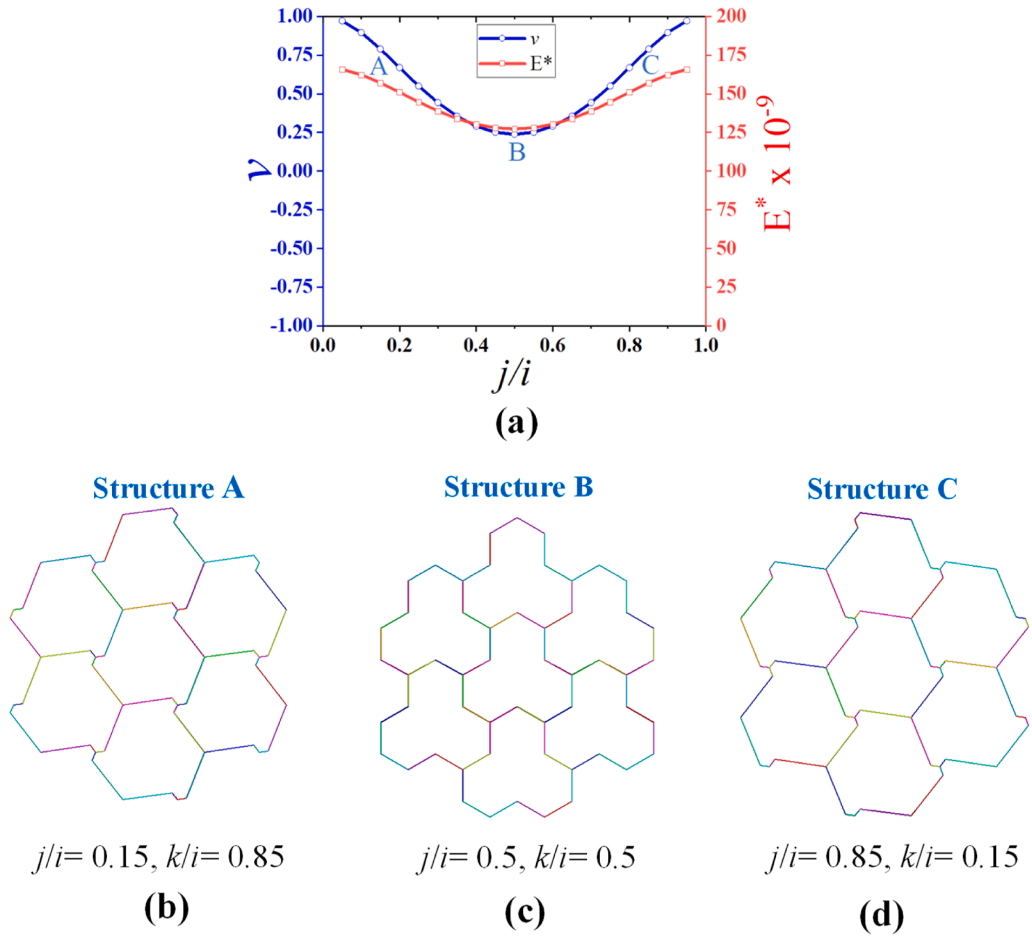

Fig. 5. Variation of Poisson's ratio and effective Young's modulus for combinations along boundary line L_1 within the i-constant set of Design I, along with the geometric configurations of three representative structures labeled A, B, and C; a) Along line L_1, both Poisson's ratio and Young's modulus exhibit symmetrical behavior with respect to midpoint B, such that both properties increase as the configuration shifts away from B toward the boundary points A and C; b) representative structure for point A with $j/i = 0.15$, and $k/i = 0.85$, c) representative structure for point B with $j/i = 0.5$, and $k/i = 0.5$, and d) representative structure for point C with $j/i = 0.85$, and $k/i = 0.15$.

lengths k remain unchanged, the new side jj replaces the original sides with length j and the sides of length i are both removed.

Similarly to Design II, the Poisson's ratio of Design III varies numerically from -0.87 to $+1$ as shown in Fig. 9. However, in this case, the variations are not limited to the boundary lines, with configurations in the central regions of the plots also showing a variable Poisson's ratio. In general, the Poisson's ratio decreases and becomes highly auxetic for configurations where j is greater than i and j is greater than k, however, in this case there is not a clear cut route towards the design of auxetic tessellations with the Poisson's ratio varying in a nonlinear manner for variations in k and i. At this point it is worth mentioning that although the minimum Poisson's ratio obtained from the original parametric simulation run is -0.87, lower values can also be obtained for configurations on the boundary line. One such example of a system exhibiting a Poisson's ratio -0.98 is shown in Fig. 10 below, where the following combination of parameters was tested: $i = 24$, $j/i = 0.998$, $k/i = 0.002$ and $t/i = 2.08 \times 10^{-4}$. It is immediately apparent that this configuration assumes a shape similar to triangular tessellation with small chiral nodes at the edges. This results in a deformation mode reminiscent of a hexachiral honeycomb which is known to exhibit a Poisson's ratio of -1 [69]. On the other hand, the positive Poisson's ratio system shown in Fig. 10 is similar to hexagonal honeycomb with small triangles at three of its vertices. As illustrated in the figure, its deformation mode is also similar to a regular hexagonal honeycomb, hence, the highly positive Poisson's ratio close to $+1$.

Fig. 11 shows the variation of mechanical properties along the boundary line L_1 in the i-constant plot in Fig. 9. For the Poisson's ratio, it is evident that the systems become more auxetic as the triangle of the tessellation becomes larger in size, which corresponds to an increase in the j-length. In addition, this also results in a significant increase in stiffness, with the effective Young's modulus also increasing as j becomes larger.

3.1.4. Comparative analysis of all tessellations

In this section, we aim to elucidate the differences in mechanical responses between the newly designed structures and their underlying hexagonal tessellation through a representative example. To this end, a common set of side lengths ($i = 24$, $j = 16$, and $k = 8$) for all the designs was selected, and the corresponding mechanical properties of each design were analyzed. The selected combination belongs to the i-constant set and are located on the boundary line L_1 (see Figs. 3, 6, and 9). The undeformed and deformed shapes of the original hexagonal system alongside the three newly designed structures developed from the original configuration with identical side lengths are illustrated in Fig. 12. The original hexagonal structure exhibits a Poisson's ratio of zero. In contrast, the three newly designed systems demonstrate distinctly diverse values as well as deformation mechanisms. Specifically, Design I has a Poisson's ratio of $+0.38$, Design II, -0.61 and Design III -0.50. These values can all be explained in terms of the deformation mechanisms described in the individual sections for all three new tessellations. In the case of Design I, the system is deforming similar to a regular hexagon, hence resulting in a positive Poisson's

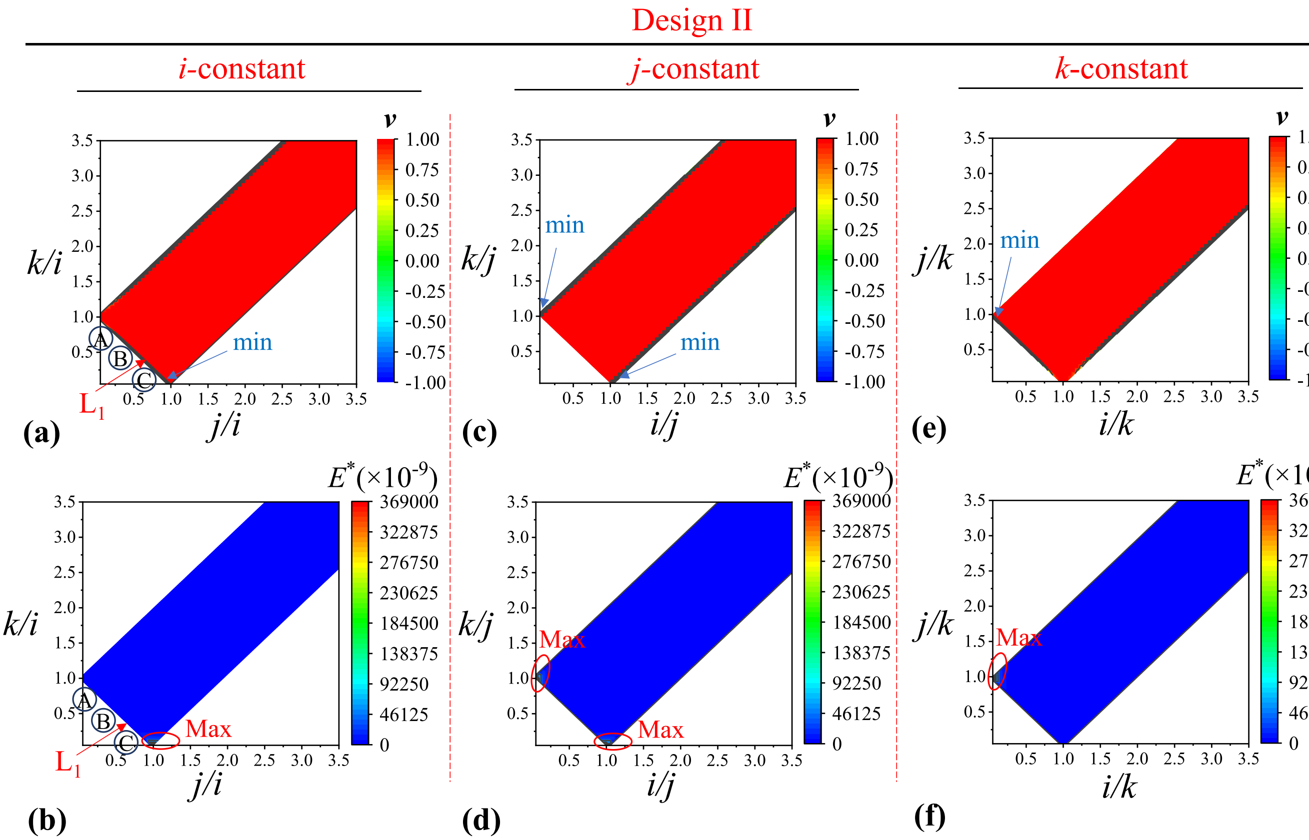

Fig. 6. Variation of Poisson's ratio and effective Young's modulus as functions of the variable side lengths for Design II, considering *i*-, *j*-, and *k*-constant setset: a) Poisson's ratio of the *i*-constant set, with a minimum value of -0.85 for $j/i = 0.95$, $k/i = 0.05$; b) Effective Young's modulus of the *i*-constant set, with a maximum value of 368945×10^{-9} for $j/i = 1$, $k/i = 0.05$; c) Poisson's ratio of the *j*-constant set, with a minimum value of -0.85 for $i/j = 1.05$, $k/j = 0.05$; $i/j = 0.05$, $k/j = 1.05$; d) Effective Young's modulus of the *j*-constant set, with a maximum value of 368945×10^{-9} for $i/j = 1$, $k/j = 0.05$ and $i/j = 0.05$, $k/j = 1$; e) Poisson's ratio of *k*-constant set, with a minimum value of -0.85 for $i/k = 0.05$, $j/k = 0.95$; f) Effective Young's modulus of *k*-constant set, with a maximum value of 368945×10^{-9} for $i/k = 0.05$, $j/k = 1$.

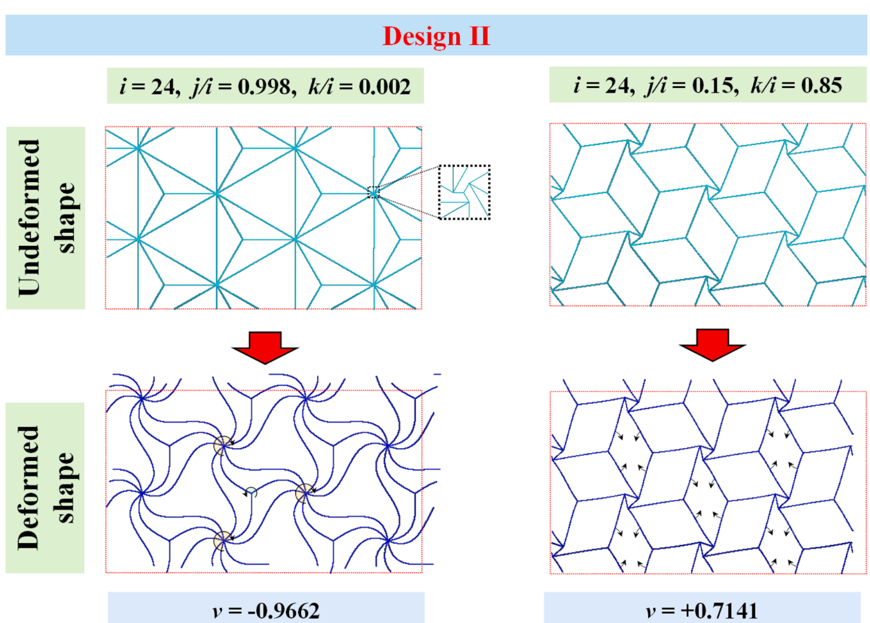

Fig. 7. Images showing the undeformed and deformed shapes of two Design II systems with *i*-constant showing a negative and positive Poisson's ratio. For the negative Poisson's ratio's system, the in-plane ligament thickness, *t*, is 0.005 mm while in the positive Poisson's ratio system it is 0.1 mm. The arrows indicate the direction of deformation of the ligaments and the systems are shown with 2 × 2 representative unit cells in order to demonstrate clearly the deformation mechanism.

ratio, while in Designs II and III, the deformations modes are mixed variants of the two mechanisms indicated in Figs. 7 and 10 for negative

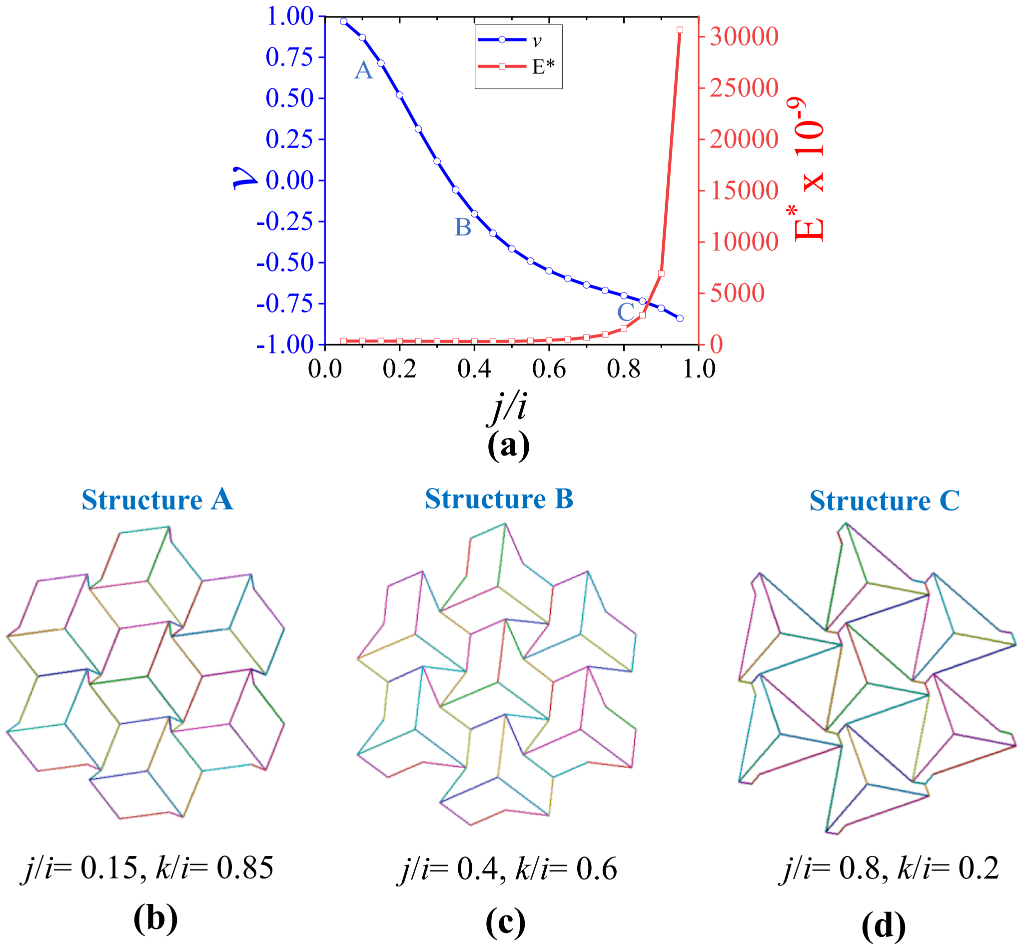

Fig. 8. Variation of Poisson's ratio and effective Young's modulus for combinations along boundary line L_1 within the *i*-constant set of Design II, along with the geometric configurations of three representative structures labeled A, B, and C; a) general trends along line L_1, showing a decrease in Poisson's ratio and an increase in effective Young's modulus, b) representative structure for point A with $j/i = 0.15$, and $k/i = 0.85$, c) representative structure for point B with $j/i = 0.4$, and $k/i = 0.6$, and d) representative structure for point C with $j/i = 0.8$, and $k/i = 0.2$.

and positive Poisson's ratio systems with more similarity to the negative Poisson's ratio mode.

In terms of effective Young's modulus, considerable differences are also observed between each structure. Design II has the highest effective Young's modulus, while also showing strong auxetic behavior, closely followed by Design III with a slightly lower effective Young's modulus. In contrast, the original hexagonal structure has a significantly lower Young's modulus, while the lowest effective Young's modulus is observed in Design I, making it the most compliant structure. This result is interesting, since when it comes to the amount of material present in each tessellation, i.e. density, the original hexagonal system has the highest amount, followed by Design II, III and I respectively. This means that Designs II and III exhibit improved stiffness/density ratios and this property most probably arises from the triangulation present in these systems which are known to impart significant reinforcement in truss-based structures [70–72].

3.2. Experimental results in comparison with non-linear FE simulation results

As discussed previously, 4 AM-fabricated prototypes were tested under *quasi*-static, compressive strain conditions. As detailed in the methodology section, these structures were each based on an identical side-length combination of *i*, *j*, and *k*; specifically $i = 20$ mm, $j = 14$ mm, and $k = 6$ mm. These configurations were chosen on the basis that they encompass nearly the entire spectrum of possible Poisson's ratios. Specifically, the base hexagonal structure exhibits a Poisson's ratio with a slightly positive value, Design I demonstrates a high positive Poisson's ratio, while Designs II and III display negative values. The choice of this combination of variables was determined based on preliminary linear simulations using BEAM189 elements. Subsequently, non-linear geometric simulations were performed on all four samples using PLANE183 elements under quasi-static, compressive strain conditions in order to obtain a more accurate comparison of the deformation modes and mechanical properties. Two sets of simulations were carried out; the first set under periodic boundary conditions, similarly to the beam element simulations, while the second one was carried out under finite boundary conditions analogous to the experimental tests. In the latter set, the Poisson's ratio was extracted from the central RUC, exactly like the point-tracking analysis used to extract the Poisson's ratio of the experimental samples.

A comparison of the experimental and non-linear FE simulation results for all structures under 10% compressive loading is shown in Fig. 13. It is manifestly clear that the deformation modes predicted by FE simulations are replicated in the experimental tests for all four designs tested. Furthermore, the Poisson's ratios obtained from the experimental tests show an extremely good match with the nonlinear FE predictions. For the original hexagonal tessellation, the Poisson's ratio is predicted by both finite and infinite FE simulations to vary across a 10% strain range, slightly increasing from + 0.13 to + 0.25, a trend which is also followed in an almost identical manner by the corresponding experimental prototype. For Design I, the Poisson's ratio is almost constant at a

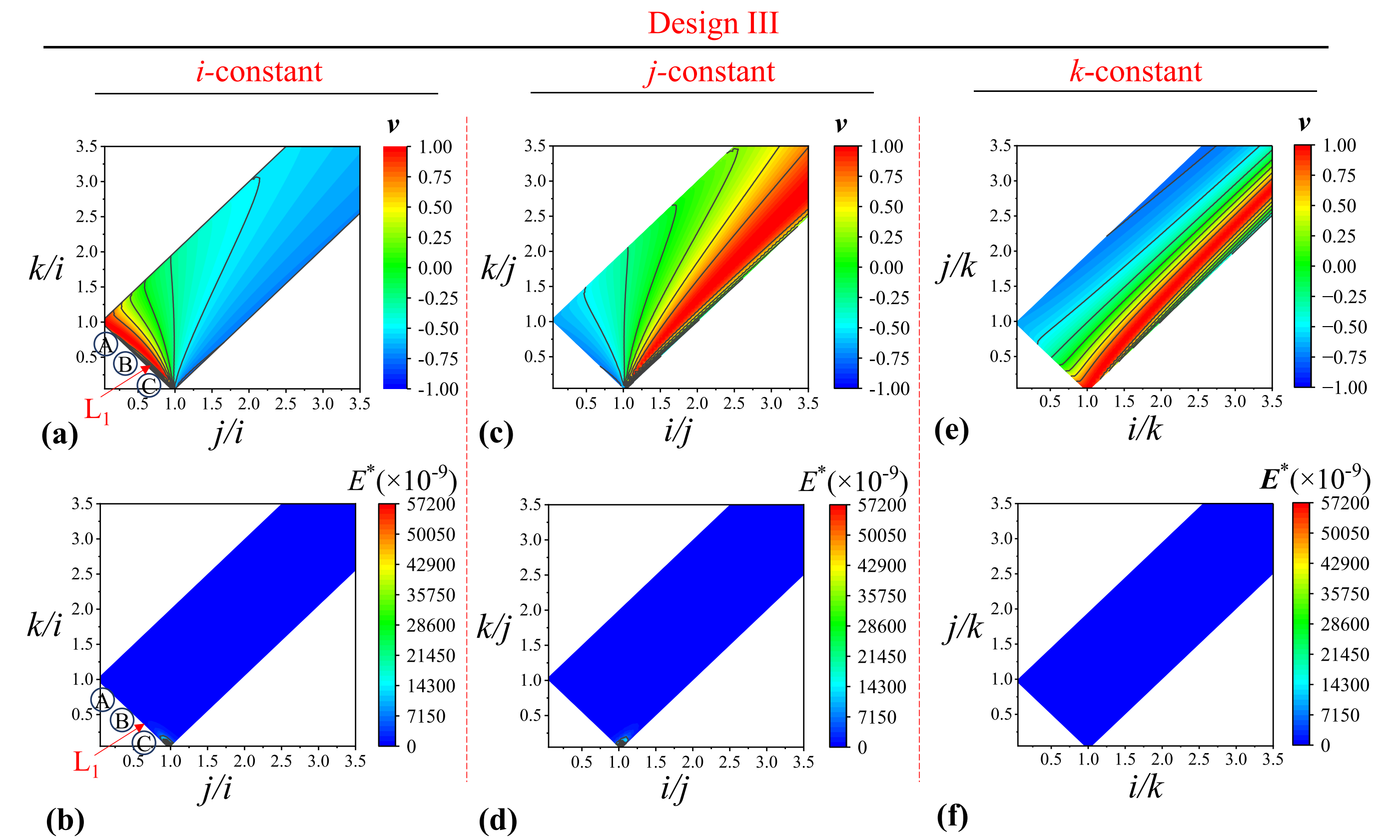

Fig. 9. Variation of Poisson's ratio and effective Young's modulus as functions of the variable side lengths for Design III, considering *i*-, *j*-, and *k*-constant setset: a) Poisson's ratio of the *i*-constant set, with a minimum value of -0.87 for $j/i = 0.95$, and $k/i = 0.05$; b) Effective Young's modulus of the *i*-constant set, with a maximum value of 57091×10^{-9} for $j/i = 1$, and $k/i = 0.05$, c) Poisson's ratio of the *j*-constant set, with a minimum value of -0.87 for $i/j = 1.05$, and $k/j = 0.05$; d) Effective Young's modulus of the *j*-constant set, with a maximum value of 57091×10^{-9} for $i/j = 1$, and $k/j = 0.05$, which corresponds to the same structure as the maximum in the *i*-constant set; e) Poisson's ratio of *k*-constant set, with a minimum value of -0.78 for $i/k = 2.55$, $j/k = 3.5$, and $i/k = 2.5$, $j/k = 3.45$; f) Effective Young's modulus of *k*-constant set, with a maximum value of 160×10^{-9} for $i/k = 1$, and $j/k = 0.05$.

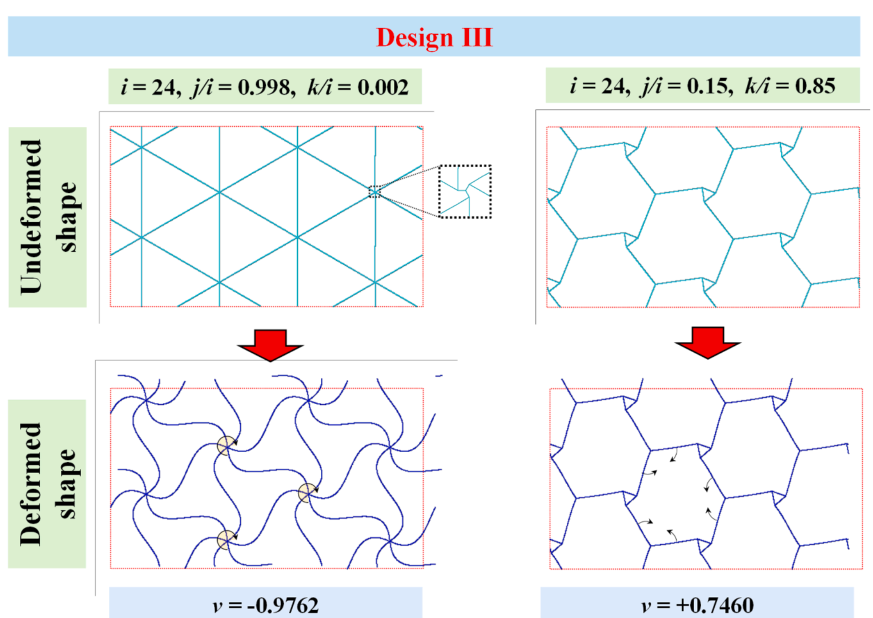

Fig. 10. Images showing the undeformed and deformed shapes of two Design III systems with *i*-constant showing a negative and positive Poisson's ratio. For the negative Poisson's ratio's system, the in-plane ligament thickness, *t*, is 0.005 mm while in the positive Poisson's ratio system it is 0.1 mm. The arrows indicate the direction of deformation of the ligaments and the systems are shown with 2 × 2 representative unit cells in order to demonstrate clearly the deformation mechanism.

value of + 0.4 and all three sets of results, i.e. experiment and two FEM simulations, show excellent agreement. In the case of Design II, which

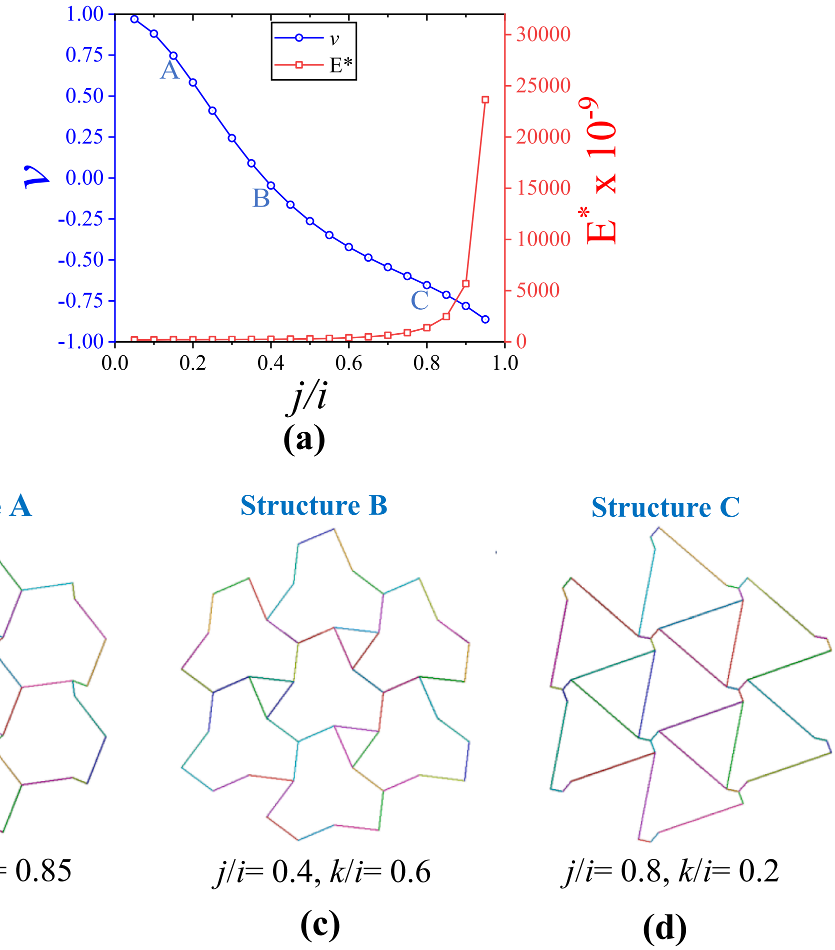

Fig. 11. Variation of Poisson's ratio and effective Young's modulus for combinations along boundary line L_1 within the *i*-constant set of Design III, along with the geometric configurations of three representative structures labeled A, B, and C; a) general trends along line L_1, showing a decrease in Poisson's ratio and an increase in effective Young's modulus, b) representative structure for point A with $j/i = 0.15$, and $k/i = 0.85$, c) representative structure for point B with $j/i = 0.4$, and $k/i = 0.6$, and d) representative structure for point C with $j/i = 0.8$, and $k/i = 0.2$.

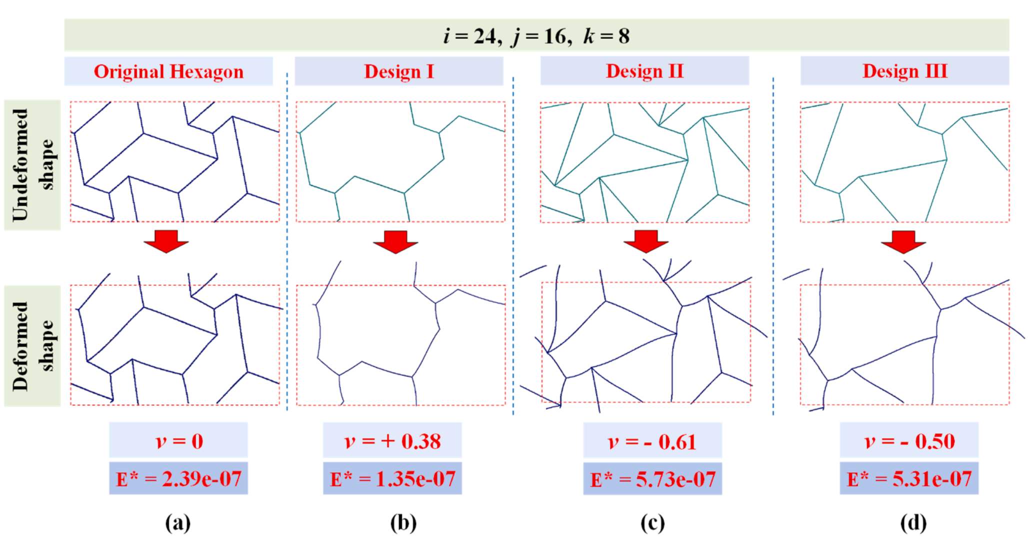

Fig. 12. Comparison of Poisson's ratio, effective Young's modulus, and deformation behaviour between the original hexagonal tessellation with side lengths of $i = 24$, $j = 16$, $k = 8$ and the three derivative Designs with the same side lengths considered in this study: a) The original hexagonal tessellation, featuring trigonal rotational symmetry and exhibiting a Poisson's ratio of $\nu = 0$; b) Design I, with $\nu = +0.38$ and the lowest effective Young's modulus; c) Design II, the most auxetic structure, with $\nu = -0.61$ and the highest effective Young's modulus; d) Design III, with $\nu = -0.50$.

exhibits auxetic behaviour, the Poisson's ratio is shown to gradually decrease in magnitude upon increasing strain for both the experimental

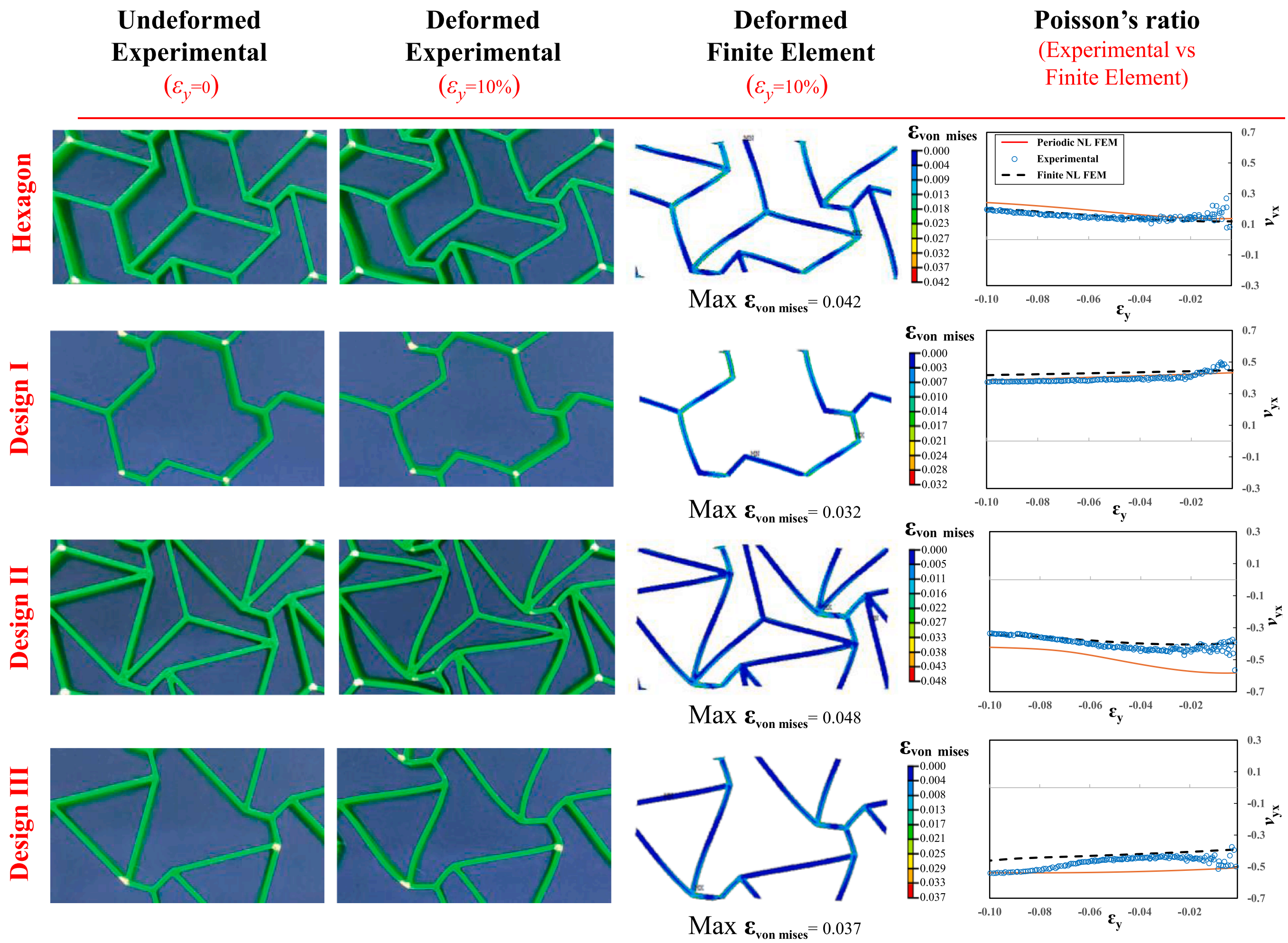

Fig. 13. Images showing the undeformed and deformed central RUCs at 10% compressive strains for the Original Hexagon, Design I, II and III along with corresponding plane element periodic FE simulations. In the plots, a comparison of the Poisson's ratio obtained from the experimental tests and the FEM simulations carried out under both periodic and finite boundary conditions are presented. All four designs were based on the following combination of parameters: $i = 20$ mm, $j = 14$ mm, and $k = 6$ mm.

prototype and FE simulations. For this system, the Poisson's ratio is predicted to be slightly lower at small strain values by the FE simulation carried out under PBCs (ca. −0.58) in comparison to the experimental system and the corresponding finite nonlinear simulation. This small discrepancy is to be expected and can be attributed to the influence of edge effects since both the experimental and finite nonlinear simulations show exactly the same trends and deformation behaviours. Finally, for Design III, which was predicted by the PBCs FE simulation to exhibit a *quasi*-constant Poisson's ratio of −0.5, both the experimental results and the finite FE simulations show a slightly higher Poisson's ratio of −0.4 at small strains which gradually decreases up to a strain of 10% to reach −0.5. This discrepancy between infinite and finite systems can also be mainly attributed to edge effects since in the simulation results the only difference between the two sets is the presence/absence of PBCs.

Another interesting point worth mentioning is the comparison of von Mises localised strain distributions between the four systems obtained from the PBCs FE simulations. This value provides an indication for the strain tolerance behaviour of these tessellations. The highest localized von Mises strain is observed for the Design II system ($\varepsilon_{von\ Mises} = 0.048$) which is also relatively the stiffest tessellation. This indicates that this system will undergo yielding or failure at lower global strain values in comparison with the other tessellations. The next highest value is observed for the Original Hexagonal system followed by Designs III and I respectively, with the latter showing a maximum $\varepsilon_{von\ Mises} = 0.032$. Overall, all of these systems showed extremely good strain tolerance behaviour, undergoing a global strain of 10% in the central RUC without failure.

3.3. General remarks and discussion

The tessellations investigated in this work have been shown to exhibit considerable versatility in terms of both Poisson's ratio and Young's modulus whilst retaining the inherent transverse isotropy associated with the trigonal rotational symmetry class. This property makes them particularly ideal for implementation as infill patterns for FDM additive manufacturing since it is possible to obtain 3D prints with a variable hierarchical framework which yields a tailored set of mechanical properties whilst retaining in-plane isotropy. In addition, all four configurations considered in this work can be designed on the basis of a small set of variables; *i*, *j* and *k* with a single common unit cell. This means that for a constrained fixed design space or infill volume, multiple configurations which possess vastly diverse mechanical properties can be fitted in. These properties can vary from high to low stiffness as well as positive to negative Poisson's ratio. Such versatility is not afforded by currently used tessellations such as monohedral regular hexagons, triangles and squares while infills based on regular dihedral tessellations, which may allow for some degree of tuneability, tend to require a relatively larger availability of space in order to fit multiple RUCs. The capability of the trigonal rotational symmetry tessellations presented in this work to exhibit the entire spectrum of permissible Poisson's ratios, which is relatively uncommon for ligament-based tessellations which are isotropic, is also unmatched by traditional tessellations as shown in Fig. 14, hence confirming the suitability of these systems for implementation as infill patterns for low density, highly-porous, cellular 3D-prints.

The next step beyond this work is to evaluate in more depth the non-linear deformation behaviour of these systems. This includes dynamic tests such as high and low velocity crushing behaviour, cyclic small-strain fatigue properties and fracture propagation and failure modes. Furthermore, studies also need to be carried out to analyse the influence of boundary effects on the mechanical performance of these tessellations, since once implemented in infills the deformation of the overall system will be inhibited to an extent by the presence of thick/thin outer walls. Finally, we hope that this work can act as a blueprint for the design and development of further infill patterns with large tuneability within the framework of a fixed global rotational symmetry. In this case, trigonal rotational symmetry tessellations were used, however, it is known from continuum mechanics and elastic theory of sheet crystals that 2D tessellations with hexagonal rotational symmetry also exhibit transverse isotropy [73,74]. Consequently, the same technique utilized here, in which a standard trigonal symmetry tessellation was altered strategically to enhance its versatility whilst retaining its original symmetry characteristics, can potentially be applied to other tessellations such as Florent Pentagonal, Deltoid Trihexagonal and Rhombille tilings [75,76] to obtain similarly promising results.

4. Conclusion

In this study, a systematic approach is presented to investigate the mechanical properties—specifically Poisson's ratio and effective Young's modulus—of structures designed through targeted geometric modifications of a hexagonal tessellation exhibiting in-plane isotropy and trigonal rotational symmetry. The proposed designs, including monohedral dodecagonal and dihedral pentagon–triangle and nonagon–triangle tessellations, were successfully derived through the controlled removal and addition of ligaments to the original hexagonal tessellation while preserving its inherent in-plane isotropy. To obtain the Poisson's ratios and Young's moduli of these tessellations, parametric linear FE simulations incorporating PBCs were conducted. The deformation behavior of structures exhibiting both negative and positive Poisson's ratios was also investigated in detail for each design. Four prototypes derived from the original hexagonal geometry, with identical variable side lengths (i, j, and k) and covering both positive and negative Poisson's ratios, were subsequently fabricated and tested through experimental compression tests, validating the FE results. All systems studied demonstrated large versatility in terms of permissible Poisson's ratios and effective stiffness values which coupled with a variable representative unit cell and volume fraction modulation potential upon changing the relative side length parameters, allows the designer a large degree of customization potential for the design 3D-printed parts with tailored porosity, Young's modulus and auxetic properties.

The main findings of this study can be summarized as follows:

- Design I—monohedral dodecagonal tessellations—exhibits Poisson's ratios in the range of $-0.55 < \nu < +1$ and has the lowest overall stiffness. For configurations with negative Poisson's ratios, the dominant deformation mechanism is rotational motion, whereas regular honeycomb-like ligament flexure governs the deformation behavior of structures exhibiting highly positive Poisson's ratios.
- Design II—dihedral pentagon–triangle tessellations—can exhibit nearly the entire spectrum of 2D isotropic Poisson's ratios, i.e., $-1 < \nu < +1$ and has the highest relative stiffness out of all three designs investigated. The auxetic response arises mainly from chiral-like rotations of short ligaments, whereas positive Poisson's ratio behavior is associated with bending deformation from the longest ligaments.
- Design III—dihedral nonagon–triangle tessellations—similar to Design II, can exhibit the full range of 2D isotropic Poisson's ratios, i.e., $-1 < \nu < +1$ and relatively high level of stiffness which is slightly lower than Design II. The dominant deformation mechanisms are rotational motion for auxetic structures and flexural deformation for non-auxetic structures, consistent with those observed in Design II.
- For each tessellation, the mechanical properties can be tailored through modifications of three side length parameters, whilst retaining at all times the transverse isotropy of the trigonal rotational symmetry class. This high level of tuneability is uncommon for isotropic tessellations and makes these systems ideal candidates for implementation as infill patterns given vast level of customizability afforded by these frameworks.

CRediT authorship contribution statement

Luke Mizzi: Writing – review & editing, Validation, Supervision, Software, Project administration, Methodology. **Andrea Spaggiari:** Validation, Resources. **Reza Moghimimonfared:** Writing – original draft, Visualization, Methodology, Investigation, Formal analysis, Conceptualization.

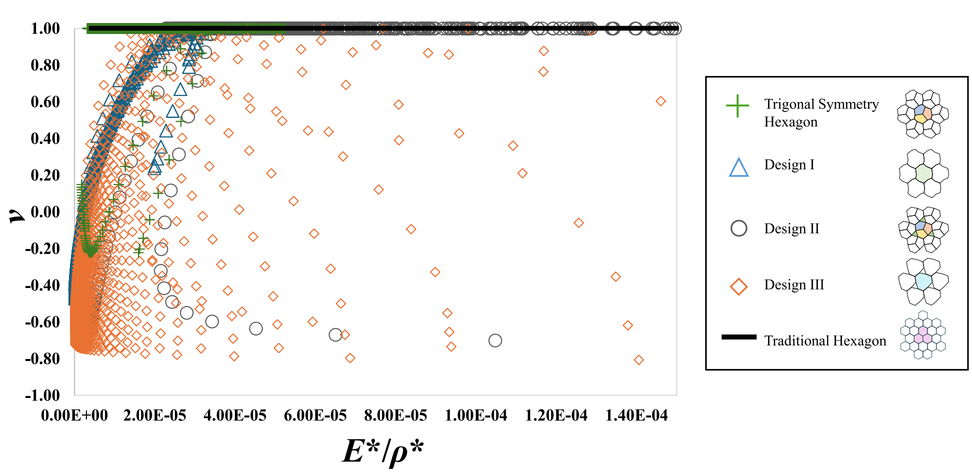

Fig. 14. Plots showing the Poisson's ratio vs effective stiffness/effective density ratio for the three new systems studied in this work: Designs I, II and III, the trigonal symmetry tessellation investigated in [63] and the traditional regular hexagonal tessellation [67] which is currently widely used as an infill pattern. The versatility of the new designs, particularly Design III with respect to regular hexagonal tilings which show a standard unchangeable Poisson's ratio of + 1 is clearly evident from the plot.

Declaration of Competing Interest

The authors declare that they have no known competing financial interests or personal relationships that could have appeared to influence the work reported in this paper.

Acknowledgements

This work was carried out within the framework of the project "A fundamental understanding of disorder in metamaterials," funded by Fondazione Cariplo and Fondazione CDP, grant no: 2023–2526, supporting young Italian researchers in ERC competitions.

Appendix A. Supporting information

Supplementary data associated with this article can be found in the online version at doi:10.1016/j.tws.2026.115088.

Data Availability

Data will be made available on request.

References

[1] T.D. Ngo, A. Kashani, G. Imbalzano, K.T.Q. Nguyen, D. Hui, Additive manufacturing (3D printing): a review of materials, methods, applications and challenges, Composites Part B Engineering 143 (2018) 172–196, https://doi.org/10.1016/j.compositesb.2018.02.012.
[2] D.W. Rosen, C.C. Seepersad, T.W. Simpson, C.B. Williams, Special issue: design for additive manufacturing: a paradigm shift in design, fabrication, and qualification, J. Mech. Des. 137 (2015) 110301, https://doi.org/10.1115/1.4031470.
[3] H. Fayazfar, M. Salarian, A. Rogalsky, D. Sarker, P. Russo, V. Paserin, et al., A critical review of powder-based additive manufacturing of ferrous alloys: process parameters, microstructure and mechanical properties, Mater. Des. 144 (2018) 98–128, https://doi.org/10.1016/j.matdes.2018.02.018.
[4] M. Pérez, D. Carou, E.M. Rubio, R. Teti, Current advances in additive manufacturing, Procedia CIRP 88 (2020) 439–444, https://doi.org/10.1016/j.procir.2020.05.076.
[5] H. Bikas, P. Stavropoulos, G. Chryssolouris, Additive manufacturing methods and modelling approaches: a critical review, Int J. Adv. Manuf. Technol. 83 (2016) 389–405, https://doi.org/10.1007/s00170-015-7576-2.
[6] R.S. Ambekar, B. Kushwaha, P. Sharma, F. Bosia, M. Fraldi, N.M. Pugno, et al., Topologically engineered 3D printed architectures with superior mechanical strength, Mater. Today 48 (2021) 72–94, https://doi.org/10.1016/j.mattod.2021.03.014.
[7] D. Acierno, A. Patti, Fused deposition modelling (FDM) of thermoplastic-based filaments: process and rheological properties—an overview, Materials 16 (2023) 7664, https://doi.org/10.3390/ma16247664.
[8] A. Cano-Vicent, M.M. Tambuwala, Sk.S. Hassan, D. Barh, A.A.A. Aljabali, M. Birkett, et al., Fused deposition modelling: current status, methodology, applications and future prospects, Addit. Manuf. 47 (2021) 102378, https://doi.org/10.1016/j.addma.2021.102378.
[9] E. Cuan-Urquizo, R. Guerra Silva, Fused filament fabrication of cellular, lattice and porous mechanical metamaterials: a review, Virtual Phys. Prototyp. 18 (2023) e2224300, https://doi.org/10.1080/17452759.2023.2224300.
[10] S. Wickramasinghe, T. Do, P. Tran, FDM-based 3D printing of polymer and associated composite: a review on mechanical properties, defects and treatments, Polymers 12 (2020) 1529, https://doi.org/10.3390/polym12071529.
[11] J. Muñoz, M. Pumera, 3D-printed biosensors for electrochemical and optical applications, TrAC Trends Anal. Chem. 128 (2020) 115933, https://doi.org/10.1016/j.trac.2020.115933.
[12] Y. Mohseni, M. Mohseni, S. Suresh, M. Riotto, A. Jaggessar, J.P. Little, et al., Investigating impacts of FDM printing parameters and geometrical features on void formation in 3D printed automotive components, Mater. Today. Proc. (2023) S2214785323034508, https://doi.org/10.1016/j.matpr.2023.06.078.
[13] Y. Lyu, H. Zhao, X. Wen, L. Lin, A.K. Schlarb, X. Shi, Optimization of 3D printing parameters for high-performance biodegradable materials, J. Appl. Polym. Sci. 138 (2021) 50782, https://doi.org/10.1002/app.50782.
[14] I.J. Solomon, P. Sevvel, J. Gunasekaran, A review on the various processing parameters in FDM, Mater. Today. Proc. 37 (2021) 509–514, https://doi.org/10.1016/j.matpr.2020.05.484.
[15] M.R. Khosravani, T. Reinicke, Effects of raster layup and printing speed on strength of 3D-printed structural components, Procedia Struct. Integr. 28 (2020) 720–725, https://doi.org/10.1016/j.prostr.2020.10.083.
[16] R. Winarso, P.W. Anggoro, R. Ismail, J. Jamari, A.P. Bayuseno, Application of fused deposition modeling (FDM) on bone scaffold manufacturing process: A review, Heliyon 8 (2022) e11701, https://doi.org/10.1016/j.heliyon.2022.e11701.
[17] S. Sahoo, H. Sutar, P. Senapati, B. Shankar Mohanto, P. Ranjan Dhal, S. Kumar Baral, Experimental investigation and optimization of the FDM process using PLA, Mater. Today. Proc. 74 (2023) 843–847, https://doi.org/10.1016/j.matpr.2022.11.208.
[18] A. Rodríguez-Panes, J. Claver, A.M. Camacho, The influence of manufacturing parameters on the mechanical behaviour of PLA and ABS pieces manufactured by FDM: a comparative analysis, Materials 11 (2018) 1333, https://doi.org/10.3390/ma11081333.
[19] I. Durgun, R. Ertan, Experimental investigation of FDM process for improvement of mechanical properties and production cost, Rapid Prototyp. J. 20 (2014) 228–235, https://doi.org/10.1108/RPJ-10-2012-0091.
[20] V.V. Gholkar, Effect of infill parameters on time, material length, weight and price in 3d printing, Int. J. Sci. Res. 6 (2020).
[21] R. Guan, D. Smith, Influence of infill parameters on the tensile mechanical properties of 3D printed parts, J. Emerg. Invest (2020), https://doi.org/10.59720/20-052.
[22] C. Lubombo, M.A. Huneault, Effect of infill patterns on the mechanical performance of lightweight 3D-printed cellular PLA parts, Mater. Today Commun. 17 (2018) 214–228, https://doi.org/10.1016/j.mtcomm.2018.09.017.
[23] A. Al Rashid, M. Koç, Experimental validation of numerical model for thermomechanical performance of material extrusion additive manufacturing process: effect of infill design & density, Results Eng. 17 (2023) 100860, https://doi.org/10.1016/j.rineng.2022.100860.
[24] R. Lakes, Foam structures with a negative poisson's rtaio, Science 235 (1987) 1038–1040.
[25] K.E. Evans, M.A. Nkansah, I.J. Hutchinson, S.C. Rogers, Molecular network design, 124–124, Nature 353 (1991), https://doi.org/10.1038/353124a0.
[26] K.E. Evans, A. Alderson, Auxetic materials: functional materials and structures from lateral thinking!, Adv. Mater. 12 (2000) 617–628, https://doi.org/10.1002/(SICI)1521-4095(200005)12:9%253C617::AID-ADMA617%253E3.0.CO;2-3.
[27] W. Liu, F. Li, Y. Liang, E. Li, D. Shou, B. Li, Three-dimensional double negative mechanical metamaterials with tailored anisotropy, Virtual Phys. Prototyp. 20 (2025) e2500669, https://doi.org/10.1080/17452759.2025.2500669.
[28] T. Li, Y. Chen, X. Hu, Y. Li, L. Wang, Exploiting negative Poisson's ratio to design 3D-printed composites with enhanced mechanical properties, Mater. Des. 142 (2018) 247–258, https://doi.org/10.1016/j.matdes.2018.01.034.
[29] T. Li, F. Liu, L. Wang, Enhancing indentation and impact resistance in auxetic composite materials, Composites Part B Engineering 198 (2020) 108229, https://doi.org/10.1016/j.compositesb.2020.108229.
[30] T. Omura, M. Kato, M. Abe, T. Sumigawa, Programmable fracture toughness in architected mechanical metamaterials, Mater. Today (2025) S1369702125005164, https://doi.org/10.1016/j.mattod.2025.11.038.
[31] K.E. Evans, A. Alderson, F.R. Christian, Auxetic two-dimensional polymer networks. An example of tailoring geometry for specific mechanical properties, Faraday Trans. 91 (1995) 2671, https://doi.org/10.1039/ft9959102671.
[32] W. Zhang, Z. Li, J. Wang, F. Scarpa, X. Wang, Mechanics of novel asymmetrical re-entrant metamaterials and metastructures, Compos. Struct. 291 (2022) 115604, https://doi.org/10.1016/j.compstruct.2022.115604.
[33] J.N. Grima, R. Gatt, A. Alderson, K.E. Evans, On the potential of connected stars as auxetic systems, Mol. Simul. 31 (2005) 925–935, https://doi.org/10.1080/08927020500401139.
[34] Z. Dong, Y. Li, T. Zhao, W. Wu, D. Xiao, J. Liang, Experimental and numerical studies on the compressive mechanical properties of the metallic auxetic reentrant honeycomb, Mater. Des. 182 (2019) 108036, https://doi.org/10.1016/j.matdes.2019.108036.
[35] A.M. Caporale, A. Airoldi, N. Novak, A novel body centered cubic 3D auxetic chiral geometry, Smart Mater. Struct. 34 (2025) 015050, https://doi.org/10.1088/1361-665X/ad9dc9.
[36] L. Mizzi, A. Spaggiari, Chiralisation of Euclidean polygonal tessellations for the design of new auxetic metamaterials, Mech. Mater. 153 (2021) 103698, https://doi.org/10.1016/j.mechmat.2020.103698.
[37] L. Mizzi, L. Grasselli, A. Spaggiari, R. Gatt, P.-S. Farrugia, J.N. Grima, Design of isotropic 2D chiral metamaterials based on monohedral pentagonal tessellations, Thin-Walled Struct. 187 (2023) 110739, https://doi.org/10.1016/j.tws.2023.110739.
[38] L. Mizzi, A. Simonetti, A. Spaggiari, Mechanical properties and failure modes of additively-manufactured chiral metamaterials based on Euclidean tessellations: an experimental and finite element study, RPJ 30 (2024) 59–71, https://doi.org/10.1108/RPJ-06-2023-0190.
[39] R. Hou, P. Dong, J. Hu, Z. Gong, S. Sadeghzade, J. Cao, et al., An optimized lozenge-chiral auxetic metamaterial with tunable auxeticity and stiffness, Mater. Des. 237 (2024) 112530, https://doi.org/10.1016/j.matdes.2023.112530.
[40] A. Alderson, K.L. Alderson, D. Attard, K.E. Evans, R. Gatt, J.N. Grima, et al., Elastic constants of 3-, 4- and 6-connected chiral and anti-chiral honeycombs subject to uniaxial in-plane loading, Compos. Sci. Technol. 70 (2010) 1042–1048, https://doi.org/10.1016/j.compscitech.2009.07.009.
[41] J.N. Grima, K.E. Evans, Auxetic behavior from rotating triangles, J. Mater. Sci. 41 (2006) 3193–3196, https://doi.org/10.1007/s10853-006-6339-8.
[42] D. Attard, J.N. Grima, A three-dimensional rotating rigid units network exhibiting negative Poisson's ratios, Phys. Status Solidi (b) 249 (2012) 1330–1338, https://doi.org/10.1002/pssb.201084223.
[43] J. N. Grima, R. Gatt, A. Alderson, K. E. Evans, On the auxetic properties of `rotating rectangles' with different connectivity, J. Phys. Soc. Jpn 74 (2005) 2866–2867, https://doi.org/10.1143/JPSJ.74.2866.
[44] Z.-Y. Li, X.-T. Wang, L. Ma, L.-Z. Wu, L. Wang, Auxetic and failure characteristics of composite stacked origami cellular materials under compression, Thin-Walled Struct. 184 (2023) 110453, https://doi.org/10.1016/j.tws.2022.110453.

[45] S. Tomita, K. Shimanuki, H. Nishigaki, S. Oyama, T. Sasagawa, D. Murai, et al., Origami-inspired metamaterials with switchable energy absorption based on bifurcated motions of a Tachi-Miura polyhedron, Mater. Des. 225 (2023) 111497, https://doi.org/10.1016/j.matdes.2022.111497.
[46] M.A. Bagheri, C.E. Aubin, M.L. Nault, I. Villemure, Mechanical characterization of an origami-inspired super deformable metamaterial with high tunability for tissue engineering, Mater. Des. 251 (2025) 113701, https://doi.org/10.1016/j.matdes.2025.113701.
[47] T. Lim, Analogies across auxetic models based on deformation mechanism, Phys. Rapid Res. Ltrs 11 (2017) 1600440, https://doi.org/10.1002/pssr.201600440.
[48] X. Ren, R. Das, P. Tran, T.D. Ngo, Y.M. Xie, Auxetic metamaterials and structures: a review, Smart Mater. Struct. 27 (2018) 023001, https://doi.org/10.1088/1361-665X/aaa61c.
[49] K.K. Dudek, M. Kadic, C. Coulais, K. Bertoldi, Shape Morphing Metamaterials (2025), https://doi.org/10.48550/arXiv.2501.14804.
[50] M. Kadic, G.W. Milton, M. van Hecke, M. Wegener, 3D metamaterials, Nat. Rev. Phys. 1 (2019) 198–210.
[51] R. Gatt, L. Mizzi, J.I. Azzopardi, K.M. Azzopardi, D. Attard, A. Casha, et al., Hierarchical Auxetic Mechanical Metamaterials, Sci. Rep. 5 (2015) 8395, https://doi.org/10.1038/srep08395.
[52] Y. Cho, J.-H. Shin, A. Costa, T.A. Kim, V. Kunin, J. Li, et al., Engineering the shape and structure of materials by fractal cut, Proc. Natl. Acad. Sci. USA 111 (2014) 17390–17395, https://doi.org/10.1073/pnas.1417276111.
[53] C. Coulais, A. Sabbadini, F. Vink, M. van Hecke, Multi-step self-guided pathways for shape-changing metamaterials, Nature 561 (2018) 512–515, https://doi.org/10.1038/s41586-018-0541-0.
[54] T.Y. Kim, S.-H. Park, K. Park, Development of functionally graded metamaterial using selective polymerization via digital light processing additive manufacturing, Addit. Manuf. 47 (2021) 102254, https://doi.org/10.1016/j.addma.2021.102254.
[55] K.K. Dudek, L. Mizzi, J.A. Iglesias Martínez, A. Spaggiari, G. Ulliac, R. Gatt, et al., Micro-scale graded mechanical metamaterials exhibiting versatile Poisson's ratio, Compos. Struct. 319 (2023) 117151, https://doi.org/10.1016/j.compstruct.2023.117151.
[56] J.N. Grima, S. Winczewski, L. Mizzi, M.C. Grech, R. Cauchi, R. Gatt, et al., Tailoring graphene to achieve negative Poisson's ratio properties, Adv. Mater. 27 (2015) 1455–1459, https://doi.org/10.1002/adma.201404106.
[57] M. Montanari, R. Moghimimonfared, A. Spaggiari, L. Mizzi, Inherently disordered auxetic metamaterials, Adv. Sci. (2026) e21908, https://doi.org/10.1002/advs.202521908.
[58] R.J. Moat, D.J. Clarke, F. Carter, D. Rust, I. Jowers, A class of aperiodic honeycombs with tuneable mechanical properties, Appl. Mater. Today 37 (2024) 102127, https://doi.org/10.1016/j.apmt.2024.102127.
[59] M.J. Mirzaali, A.A. Zadpoor, Orthopedic meta-implants, APL Bioeng. 8 (2024) 010901, https://doi.org/10.1063/5.0179908.
[60] R. Hasanzadeh, S. Jolaiy, M. Mojaver, T. Azdast, C.B. Park, Auxetic 3D printed metastructure stents for enhanced mechanical and structural performance and biocompatibility in coronary artery treatments, Acta Biomater. 202 (2025) 641–659, https://doi.org/10.1016/j.actbio.2025.06.043.
[61] X. Zhu, J. Zhang, W. Chen, H. Gu, Tension-twist coupling morphing wing using a novel mechanical metamaterial, Aerosp. Sci. Technol. 155 (2024) 109745, https://doi.org/10.1016/j.ast.2024.109745.
[62] A. Rafsanjani, K. Bertoldi, A.R. Studart, Programming soft robots with flexible mechanical metamaterials, Sci. Robot 4 (2019) eaav7874, https://doi.org/10.1126/scirobotics.aav7874.
[63] Moghimimonfared R., Spaggiari A., Grasselli L., Mizzi L. Hexagonal Tessellation-Based Mechanical Metamaterials 2025. https://doi.org/10.2139/ssrn.5193531.
[64] Barlat F., Lian J. ANSYS Mechanical APDL Element Reference n.d.
[65] L. Mizzi, D. Attard, R. Gatt, K.K. Dudek, B. Ellul, J.N. Grima, Implementation of periodic boundary conditions for loading of mechanical metamaterials and other complex geometric microstructures using finite element analysis, Eng. Comput. 37 (2021) 1765–1779, https://doi.org/10.1007/s00366-019-00910-1.
[66] P. Suquet, Homogenization techniques for composite media, Springer, Berlin, 1987.
[67] L.J. Gibson, M.F. Ashby, S.G. Schajer, C.I. Robertson, The mechanics of two-dimensional cellular materials, Proc. R. Soc. Part A 382 (1982) 25–42.
[68] Timoshenko S.P. Theory of Elasticity 1970.
[69] D. Prall, R.S. Lakes, Properties of a chiral honeycomb with a poisson's ratio of — 1, Int. J. Mech. Sci. 39 (1997) 305–314, https://doi.org/10.1016/S0020-7403(96)00025-2.
[70] M.F. Ashby, The properties of foams and lattices, Philos. Trans. R. Soc. A 364 (2006) 15–30, https://doi.org/10.1098/rsta.2005.1678.
[71] D. Rayneau-Kirkhope, Stiff auxetics: Hierarchy as a route to stiff, strong lattice based auxetic meta-materials, Sci. Rep. 8 (2018) 12437, https://doi.org/10.1038/s41598-018-30822-x.
[72] L. Mizzi, A. Spaggiari, Lightweight mechanical metamaterials designed using hierarchical truss elements, Smart Mater. Struct. 29 (2020) 105036, https://doi.org/10.1088/1361-665X/aba53c.
[73] E. Gao, R. Li, S. Fang, Q. Shao, R.H. Baughman, Bounds on the in-plane Poisson's ratios and the in-plane linear and area compressibilities for sheet crystals, J. Mech. Phys. Solids 152 (2021), https://doi.org/10.1016/j.jmps.2021.104409.
[74] T.C.T. Ting, Poisson's ratio for anisotropic elastic materials can have no bounds, Q J. Mech. Appl. Math. 58 (2005) 73–82.
[75] B. Grunbum, G. Shephard, Tilings and Patterns, Dover Books, 1987.
[76] J.H. Conway, H. Burgiel, C. Goodman-Strauss, The Symmetries of Things, Taylor Fr. Group (2008).